Mutagenesis and Modeling of the Peroxiredoxin (Prx) Complex with the NMR Structure of ATP-Bound Human Sulfiredoxin Implicate Aspartate 187 of Prx I as the Catalytic Residue in ATP Hydrolysis‡

Duck-Yeon Lee,§ Sung Jun Park,§ Woojin Jeong,|| Ho Jin Sung,|| Taena Oho,|| Xiongwu Wu,⊥ Sue Goo Rhee,§,|| and James M. Gruschus*,⊥

Laboratory of Cell Signaling and Laboratory of Computational Biology, National Heart, Lung, and Blood Institute, National Institutes of Health, Bethesda, Maryland 20892-0301, and Division of Molecular Life Sciences, Ewha Womans University, Seoul, Korea 120-750

Received August 31, 2006; Revised Manuscript Received October 24, 2006

ABSTRACT: The catalytic cysteine of certain members of the peroxiredoxin (Prx) family can be hyperoxidized to cysteinesulfinic acid during reduction of peroxides. Sulfiredoxin is responsible for the ATP-dependent reduction of cysteinesulfinic acid (SO_2H) of hyperoxidized Prx. Here we report the NMR solution structure of human sulfiredoxin (hSrx), both with and without bound ATP, and we model the complex of ATP-bound hSrx with Prx. Binding ATP causes only small changes in the NMR structure of hSrx, and the bound ATP conformation is quite similar to that seen for the previously reported X-ray structure of the ADP−hSrx complex. Although hSrx binds ATP, it does not catalyze hydrolysis by itself and has no catalytic acid residue typical of most ATPase and kinase family proteins. For modeling the complex, the ATP-bound hSrx was docked to hyperoxidized Prx II using EMAP of CHARMM. In the model complex, Asn186 of Prx II (Asp187 of Prx I) is in contact with the hSrx-bound ATP β- and γ-phosphate groups. Asp187 of Prx I was mutated to alanine and asparagine, and binding and activity of the mutants with hSrx were compared to those of the wild type. For the D187N mutant, both binding and hydrolysis and reduction activities were comparable to those of the wild type, whereas for D187A, binding was unimpaired but ATP hydrolysis and reduction did not occur. The modeling and mutagenesis analyses strongly implicate Asp187 of Prx I as the catalytic residue responsible for ATP hydrolysis in the cysteinesulfinic acid reduction of Prx by hSrx.

Peroxiredoxins (Prx) make up a family of peroxidases that catalyze the reduction of H_2O_2, peroxynitrite, and hydroperoxides (*1*, *2*). Members of the two-Cys subfamily of Prx contain two critical cysteine residues, the peroxidatic cysteine, which is selectively oxidized as the first step in catalysis, and the resolving cysteine that reacts with the sulfenic form peroxidatic cysteine to form a disulfide. The disulfide can then be reduced by cellular antioxidant systems such as glutathione or thioredoxin, completing the cycle. Occasionally, the peroxidatic cysteine is hyperoxidized to cysteinesulfinic acid by H_2O_2 (*3*). This reaction was once thought to be irreversible, but it is now known that the protein sulfiredoxin (Srx) reduces cysteinesulfinic acid to cysteine in eukaryotes utilizing ATP (*4*). Figure 1 shows a schematic diagram of these Prx and Srx reactions. Because the reaction is reversible in the cell, it is plausible that cysteinesulfinic acid formation might be part of a sensor system for oxidative stress via regulation of post-translational modification of Prx.

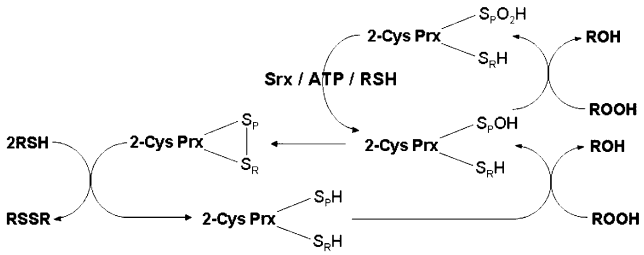

FIGURE 1: Schematic diagram of 2-Cys Prx cysteine oxidation and reduction, including reduction of cysteinesulfinic acid by Srx. S_P and S_R are the peroxidatic and resolving cysteine sulfurs, respectively, ROOH is a peroxide, and RSH is an antioxidizing agent such as glutathione or thioredoxin.

Mounting evidence suggests that H_2O_2-eliminating enzymes are extensively regulated through post-translational modification (*5*).

Human sulfiredoxin (hSrx) is a 14 kDa protein ubiquitously expressed at various levels in human tissues, capable of reducing the active site Prx cysteinesulfinic acid to cysteine (desulfinylation) using not only ATP but also GTP (*6*). To better understand the reduction mechanism, we have performed NMR studies and biochemical analysis. In this paper, we report the tertiary structure of both free and ATP-bound hSrx. Protein−protein docking of hSrx to the Prx decamer was performed with EMAP, part of CHARMM.

‡ PDB entries 1YZS and 2B6F. BMRB NMR assignment file 6590.

* To whom correspondence should be addressed. Phone: (301) 496-2350. Fax: (301) 402-3404.

§ Laboratory of Cell Signaling, National Heart, Lung, and Blood Institute, National Institutes of Health.

|| Ewha Womans University.

⊥ Laboratory of Computational Biology, National Heart, Lung, and Blood Institute, National Institutes of Health.

10.1021/bi061824h
Published on Web 12/05/2006

EMAP, a grid-based approach which uses maps of molecular properties instead of an explicit atomic description, was developed to efficiently handle large macromolecular systems (*7*, *8*). Our biochemical results and the modeling of the hSrx−Prx complex suggest that Prx provides the catalytic aspartic acid (or asparagine for Prx II) for stimulating ATP hydrolysis during the reduction of hyperoxidized Prx.

MATERIALS AND METHODS

Protein Expression and Purification. HSrx and Prx I were prepared as described in ref *6*. Prx I mutants were made using the QuickChangeII site-directed mutagenesis kit (Stratagene). Uniformly ^{15}N-labeled and ^{13}C- and ^{15}N-labeled hSrx were obtained as described previously (*9*). For the NMR structure determination, hSrx lacking the 16 N-terminal amino acids (hSrx-ΔN16) was used due to its superior solubility (*9*). Proper folding of hSrx-ΔN16 compared to that of the full-length protein was confirmed by circular dichroism (CD), and sulfinic acid reduction activity was confirmed (Figure 1 of the Supporting Information).

NMR Experiments. NMR samples consisted of 2.5 mg of hSrx protein in 250 μL (750 μM) with 50 mM potassium phosphate (pH 7.0), 100 mM NaCl, and 2 mM DTT. All three-dimensional (3D) spectra were recorded on a Bruker 800 MHz Avance spectrometer with a TXI triple-axis gradient probe at 300 K for hSrx both with and without ATP (20 mM). Experiments include 3D ^{15}N-edited NOESY-HSQC (t_{mix} = 100 ms) with a 45° water flip back (*10*), 3D short constant time (2.7 ms) ^{13}C-edited NOESY-HSQC (^{13}C carrier at 40 ppm; t_{mix} = 100 ms) (*11*) with sensitivity enhancement (*12*), and ^{13}C-edited NOESY-HMQC (^{13}C carrier at 125 ppm; t_{mix} = 100 ms) (*13*) with water flip back (*14*) and WATERGATE water suppression (*15*). All two-dimensional (2D) ^{15}N HSQC spectra for the ATP and ADP titrations were recorded at 300 K on a Bruker 600 MHz Avance spectrometer equipped with a cryoprobe. The concentration of ATP and ADP used in the nucleotide titrations was estimated with an ϵ_{259} of 15 300 M^{-1} cm^{-1}. ATP and ADP titrations were carried out by adding small aliquots of concentrated nucleotide solutions to a solution of 250 μM apo hSrx and collecting 2D ^{1}H−^{15}N HSQC spectra with increasing nucleotide concentrations of 0, 0.1, 0.3, 0.6, 1.2, 2.4, 4.8, 9.6, and 19.2 mM. The changes in backbone amide shifts in the ^{1}H−^{15}N HSQC spectra were calculated using the combined chemical shift difference, $\Delta\delta$(NH), with the equation $\Delta\delta(\mathrm{NH}) = \{[(\Delta\delta\mathrm{H})^2 + (\Delta\delta\mathrm{N}/5)^2]/2\}^{1/2}$, where $\Delta\delta$H is the ^{1}H chemical shift change and $\Delta\delta$N is the ^{15}N chemical shift change (*16*). The $\Delta\delta$(NH) values were plotted for each residue versus nucleotide concentration; the slope was calculated, and the same procedure was repeated for the backbone amide intensities. Additional NMR experiments used for chemical shift assignments are described elsewhere (*9*). nmrPipe (*17*) was used to process the spectra. Secondary structure analysis was performed using the chemical shift index (CSI) method (*18*).

Structural Restraint Determination. Distance restraint generation from the NOESY spectra followed the procedure described in ref *19*. Calibration was achieved using log−log plots of expected distance versus normalized NOE peak intensities, yielding slopes of −4.5, −5.5, and −6.0 for the ^{15}N, aliphatic ^{13}C, and aromatic ^{13}C NOESY spectra, respectively. Restraint distance ranges were determined assuming a factor of 3 deviation above or below the expected distance calculated using the calibration curves with the corresponding normalized NOE intensities. Backbone ϕ and ψ torsional angle restraints were obtained using TALOS (*20*) using ^{13}C α and β resonances supplemented by α proton and amide nitrogen and proton resonances. The ϕ and ψ restraint ranges were taken as 4 times the uncertainty range in the TALOS output file.

Structure Determination. The structure of hSrx in free and ATP-bound forms was generated using XPLOR-NIH version 2.9.7 (*21*) based on X-PLOR version 3.851 (A. Brunger, Yale University, New Haven, CT). For each form, a set of 200 structures was generated using the standard "dg_sub_embed" (backbone embedding), "dgsa" (distance geometry, simulated annealing), and "refine" (additional simulated annealing) XPLOR-NIH routines, following the procedure described in ref *19*. The ATP molecule was not included at this stage for the structure determination of the ATP-bound form. Floating chirality was employed (*22*) with relatively high initial temperatures in the dgsa and refine routines, 10 000 and 5000 K, respectively, to allow sufficient prochiral sampling. From the 200 refined structures, the 20 structures with the lowest X-PLOR energies were chosen for the final refinement steps. For the final refinement, the force constant was 30 kcal/Å^2 for the NOE restraints and 100 kcal/rad^2 for the dihedral restraints, and the van der Waals repel parameter was set to 0.80. The "sum" averaging and "square" potential options were used for the NOE restraints throughout. For the final structures, 5000 steps of minimization were performed.

The ATP molecule was docked to the ATP-bound hSrx structure by restrained molecular dynamics using MacroModel/Maestro (Schrödinger, New York, NY). The NOE cross-peaks from ATP to hSrx were sorted into three distance restraint categories: strong (0−3.4 Å), medium (3.0−4.2 Å), and weak (3.6−5.0 Å). Initially, up to 10 poses were generated for each of six lowest-energy XPLOR structures of the ATP-bound hSrx by repositioning the ATP interactively near the ATP binding site with small random translations (∼5 Å) away from the hSrx surface, and small rotations about a random axis (∼30°), and then repeating the restrained dynamics. The dynamics consisted of 10 ps of equilibration and 50 ps of stochastic dynamics (OPLS 2003 force field, 1.5 fs step, 20 Å electrostatic, 8 Å van der Waals cutoffs, GB/SA implicit water, 400 K), with the protein held fixed and a restraint strength of 100 kcal mol^{-1} Å^{-1}. A divalent cation was included, restrained to be 2−5 Å from the β-phosphorus. Each pose was then minimized along with hSrx residues within 10 Å of ATP. Poses were kept with phosphate groups <3 Å from the hSrx backbone amides of G98, C99, H100, and R101. These fell into five classes, and one ATP−hSrx complex from each class was retained for further analysis. These five representative poses were placed, one at a time, in the hSrx binding site (by superposing with the preliminary docked structure hSrx backbone) of each of the 20 XPLOR structures of ATP-bound hSrx. In addition to the restraints for observed NOE cross-peaks, repulsive restraints (>4 Å, 100 kcal mol^{-1} Å^{-1}) for hSrx protons close to H2 and H8 of the ATP base, but with no observed cross-peaks, were included at this point. Minimization was performed by MacroModel for each of the five representative complexes, with the backbone of residues >10 Å from ATP

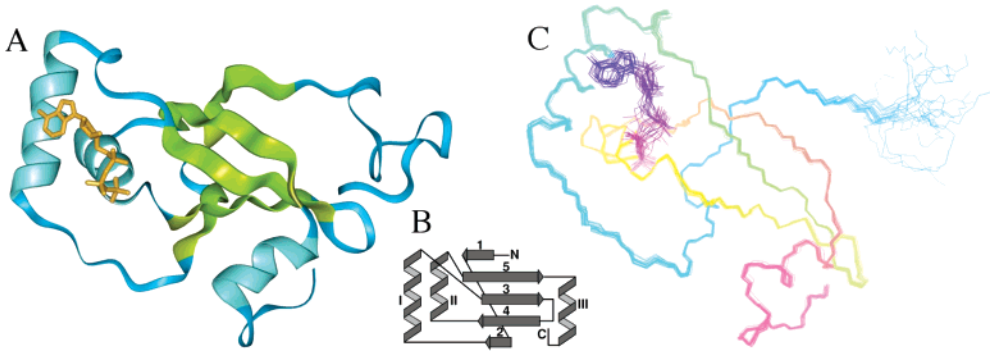

FIGURE 2: Ribbon diagram (A), topology diagram (B), and superposition of NMR structures (C) for ATP-bound hSrx. In panel C, the protein backbone is shaded from light blue at the N-terminus to pink at the C-terminus with the bound ATP shaded from blue for the base to pink for the γ-phosphate. N-Terminal residues 17−36 are flexible random coil, and residues 17−32 are not shown in the superposition.

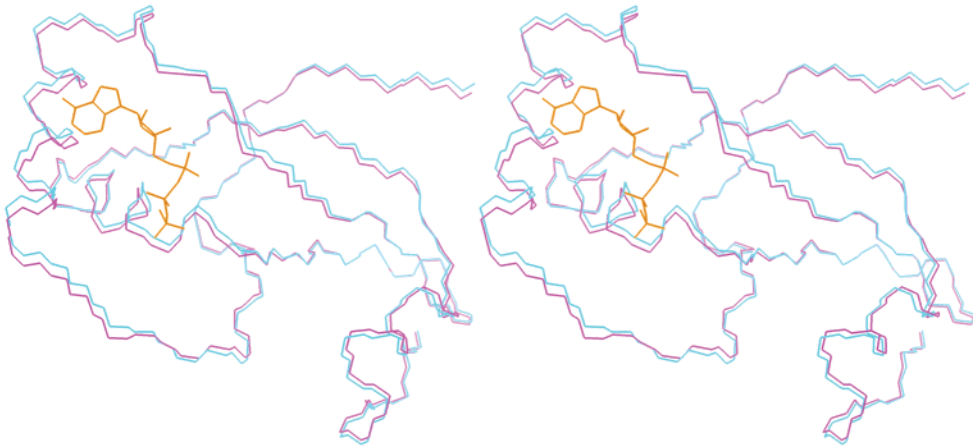

FIGURE 3: Stereoview of the average NMR structures for free (magenta) and ATP-bound (blue) hSrx with ATP colored orange.

held fixed, and the complex resulting in the lowest total energy was retained and subjected to 5000 steps of minimization in XPLOR to ensure that all experimental restraints remained satisfied.

Docking and Modeling. To create the hSrx−Prx model structures, the ATP-bound hSrx NMR structure was docked to the hyperoxidized Prx II decamer (PDB entry 1QMV) (*23*) or oxidized disulfide dimer (PDB entry 1QQ2) (*24*) using the EMAP module of CHARMM version 32. For the model complex with the hyperoxidized Prx dimer, chains A and B of the Prx decamer were used. hSrx and Prx were converted by EMAP to map objects with grid intervals of 3 Å. Default map potential parameters [dielectric constant (ϵ = 80), desolvation parameter (p_{solv} = 100 kcal/grid), surface binding parameter (p_{bind} = 300 kcal/grid), and van der Waals core parameter (p_{core} = 0.2 kcal/grid)] were used. The grid-threading Monte Carlo (GTMC) method (*7*) with 3 × 3 × 3 translational and 3 × 3 × 3 rotational MC threads was used to search minimum energy states. The local minimum complex states were stored for postdocking analysis. The bound ATP was included along with the Mg^{2+} ion. All EMAP-docked structures were saved for later ATP and cysteine distance analyses (see Results). For comparison with EMAP, hSrx was also docked to Prx II using the web-based ClusPro server (http://nrc.bu.edu/cluster) (*25*). Because of the large size of the Prx decamer, docking was performed only with the dimer (chains A and B) of the Prx II decamer. The ATP-bound hSrx structure was used, but with ATP removed, and the cysteinesulfinic acid of Prx replaced with cysteine. DOT was used for the ClusPro docking, and a clustering radius of 9 Å was employed with 1500 electrostatic hits being clustered. The 10 best docked structures were then analyzed for hSrx−Prx ATP and cysteine distances.

RESULTS

hSrx Structure. The structure for both free (PDB entry 1YZS) and ATP-bound hSrx (PDB entry 2B6F) consists of a central, five-stranded β sheet and three outlying helices, one near the C-terminus, and the other two on the opposite side of the protein, packed together at an angle of roughly 60° (Figure 2). The well-ordered structure starts with the first β strand at residue 37 and remains well structured to the end of the C-terminus. The N-terminal residues up to residue 37 exhibit sharp NMR signals and lack medium- and long-range NOE signals, typical of flexible random coil. Figure 2C shows the superposition of the 20 NMR-determined structures for the ATP-bound form, and Figure 3 shows the superposed average backbone for the free and ATP-bound forms. The hSrx structure for the ATP-bound form is very similar to the unbound form, with a backbone rms deviation of 0.51 Å. Indeed, the majority of the 3D NOE spectra cross-peaks for the unbound and bound forms are unchanged, within noise, and only 135 restraints (not including those to ATP) were altered, added, or deleted. The largest difference in the structures is seen for helix 1 (α1), which forms part of the ATP binding site, and the chemical shift differences between free and bound hSrx are greater for this helix (Figure 4). The statistics for the structure determinations are given in Table 1 of the Supporting Information, and a summary of the NMR data indicative of

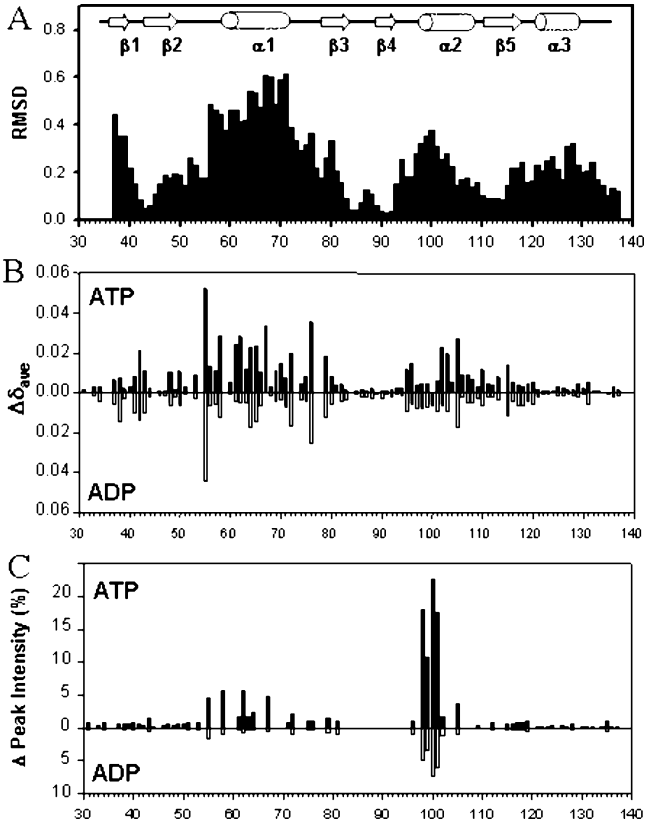

FIGURE 4: Histograms showing changes in the hSrx backbone upon binding of ATP and ADP. (A) Differences in the free and ATP-bound backbone structures (angstroms) with a secondary structure diagram. (B) Differences in the backbone amide chemical shifts per millimolar titrated ATP (top part of histogram) and ADP (bottom). (C) Percent reduction of amide ^{15}N HSQC intensity relative to nucleotide-free hSrx per millimolar titrated ATP (top) and ADP (bottom).

the secondary structure of hSrx is provided in Figure 2 of the Supporting Information.

The structure of the bound ATP was determined using NOE distance restraints to ribose and base groups. While NOE cross-peaks seen in the ^{13}C-edited NOESY-HMQC spectra between protein and ribose were unambiguous, NOE cross-peaks from the adenine base in both the ^{13}C-edited and ^{15}N-edited NOESY spectra were considerably weaker, and their assignment was aided by examining the pattern of ring current-induced shift changes in the residues surrounding the base binding site (Figure 5A). Ten ATP cross-peaks, five from the ribose and five from the base, were assigned and used as distance restraints. The resonances shifted due to ATP binding were also broadened to varying degrees, indicating conformational exchange in the base binding pocket, perhaps due to the ATP residence time falling within the intermediate NMR time scale regime (from ~100 ns to ~1 ms) (*26*). However, the ATP binding constant is not weak (6 μM) (*6*), and other possibilities are that the broadening arises due to exchange between different bound ATP conformations or increased flexibility of the protein at the nucleotide-binding site (*27*).

Additional information about the location of the phosphate contacts was obtained from an ATP titration series of ^{15}N HSQC spectra and comparison with an ADP titration series. The results are summarized in Figure 4. While the chemical shift and intensity changes are smaller overall for ADP than

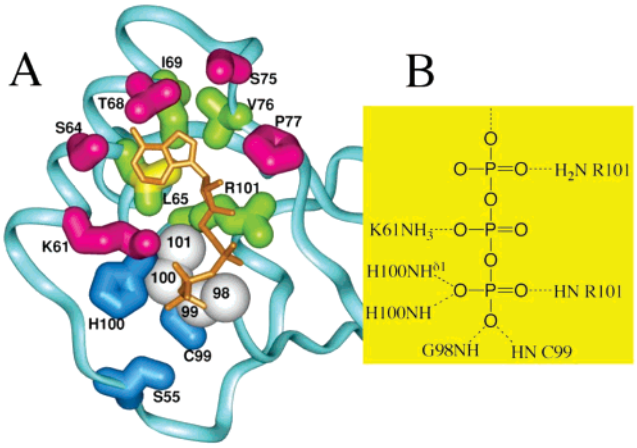

FIGURE 5: hSrx residues significantly perturbed by ATP binding. Side chains colored red had NMR resonances that were broadened and shifted downfield by ATP; green side chains were broadened and shifted upfield, and blue side chain resonances were perturbed in both field directions. The yellow side chain atoms of Leu65 and the white spheres, which correspond to backbone amides at the N-terminus of helix II, represent resonances no longer detectable due to broadening at ATP concentrations of >5 mM. Also shown is a simplified diagram of the ATP phosphate contacts.

for ATP, most likely due to weaker binding of ADP, the patterns of shift changes and intensity changes are quite similar. Many of the shift changes correlate with the structural difference seen for helix 1 when comparing the free and ATP-bound structures, suggesting that ADP and ATP binding affect helix 1 in similar ways. The greatest reductions in intensity are seen for backbone amides Gly98, Cys99, His100, and Arg101. These intensity reductions, combined with the observed ATP−hSrx NOE results, are consistent with phosphate contacts at these amides (Figures 4 and 5). Additionally, the electrostatic potential in this region, which lies at the N-terminal end of helix 2, is strongly positive (Figure 3 of the Supporting Information) and thus a favorable location for interaction with the negative phosphate groups. The patterns of intensity reduction for ATP and ADP are similar, which indicates that ATP and ADP interact with these backbone amides in a similar fashion, despite the fact that ADP is shorter by one phosphate. Even at ATP concentrations up to 20 mM, much greater than the ATP binding constant (6 μM), no reversal of intensity reduction was observed, consistent with the bound ATP or binding pocket undergoing conformational exchange on the intermediate time scale. The largest observed backbone chemical shift change is seen for Ser55 (Figure 4). The Ser55 side chain can contact the Cys99 side chain and, consequently, is not far (<7 Å) from the bound ATP (Figure 5A).

The phosphate conformations of bound ATP were generated on the basis of the working assumption that the backbone amides, Gly98, Cys99, His100, and Arg101, lie within 3 Å of at least one phosphate oxygen (see Materials and Methods). MacroModel was used instead of XPLOR for energy minimization because of its more advanced force field, which employs a generalized Born/surface area (GBSA) term to estimate the free energy of desolvation (*28*). From initial modeling, five low-energy triphosphate conformations of the bound ATP were identified (Figure 4 of the Supporting Information). In all cases, the phosphates also interacted with the side chains of Lys61, His100, and Arg101. Next, each of the five model ATP conformations was superimposed on

the 20 hSrx NMR structures and minimized to determine the lowest-energy phosphate conformation. In 18 of the 20 NMR structures, the conformation shown in Figure 5B resulted in the lowest energy (conformation 1 in Figure 4 of the Supporting Information). This conformation has the γ-phosphate positioned at the head of helix 1, contacting the four backbone amides, Gly98, Cys99, His100, and Arg101, as well as the side chain of His100.

Modeling the hSrx−Prx Complex. Attempts to crystallize a Prx−hSrx complex failed (data not shown); thus, we performed the modeling of the Prx−hSrx complex to gain further insight into the mechanism of the reduction of the cysteinesulfinic acid by hSrx. In its reduced form Prx forms a decamer, while in its disulfide form the decamer is destabilized into dimers, which are then reduced by agents such as thioredoxin (*1*, *29*, *30*). The formation of the disulfide linkage from the cysteinesulfenic intermediate is not fast, however, and increasing concentrations of H_2O_2 can lead to further oxidation of the cysteine to the sulfinic form, in which case Prx remains in the decamer form (*1*, *23*).

The Prx II decamer structure with the sulfinic acid form of the peroxidatic cysteine (*23*) and ATP-bound hSrx were docked using EMAP, part of CHARMM version 32b1 (*31*). EMAP was developed to efficiently handle large macromolecular systems and has been successfully applied to protein systems comparable in size to the Prx II decamer (*8*). Unlike traditional molecular modeling approaches that describe a molecule as a group of atoms linked with chemical bonds, EMAP uses maps to represent macromolecules, with each relatively rigid domain described as a map object (*7*). A map object neglects internal chemical structures. Instead, it represents a spatial distribution of certain properties, such as charge, density, and solvent accessibility. The flexibility of macromolecules is taken into account through the low resolution in the spatial distribution of molecular properties. Interactions between macromolecules are calculated through map potentials consisting of electrostatic, van der Waals, desolvation, and surface binding terms derived from the CHARMM force field.

EMAP performs Monte Carlo minimization of hundreds of starting structures, and the minimized docked structures were searched for those with the shortest distance between the reactive cysteine sulfur atoms of each protein, Cys99 of hSrx and Cys51 of Prx, and also the shortest distance between the ATP γ-phosphate and Cys51 of Prx. The docked complex with the shortest distances is shown in panels A and B of Figure 6, with a Cys−Cys distance of 12.2 Å and a Cys−ATP distance of 11.9 Å. In this docked conformation, the ATP phosphate groups are buried at the interface (Figure 7), and the hSrx loop containing Ser55, the residue most perturbed by ATP binding, is inserted into a large cleft on the Prx decamer surface where three Prx monomers meet (Figure 6C).

Potential interactions suggested by the model include hydrophobic, hSrx Val56 with Prx Val187 for instance, as well as electrostatic interactions, such as hSrx Asp58 with Prx Arg127. Mutation of hSrx Asp58 to Asn has been found to interfere with Prx binding (*32*). The electrostatic potential of Prx at the putative binding site has both positive and negative areas, and overall, the Prx potential is more positive toward the center of the decamer ring and negative toward the outer edge (Figure 5A of the Supporting Information),

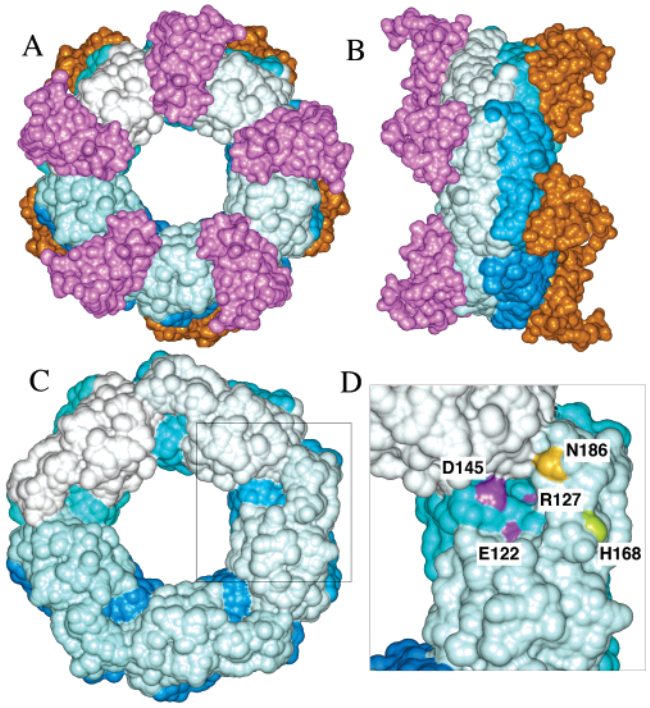

FIGURE 6: Axial view (A) of the Prx II decamer with bound hSrx predicted by EMAP and side view (B) seen from the right. The Prx monomers are shown in shades of blue, light on one side of the decamer and dark on the other, and the hSrx proteins are colored pink on one side and orange on the other. The 10 hSrx proteins shown bound to the decamer illustrate there is no contact between the bound hSrx proteins; the actual stoichiometry in the cell has not yet been determined. (C) Prx decamer shown without the bound hSrx to show the binding site lies in a pocket where three Prx monomers meet (compare with panel A). (D) Close-up of one of the binding pockets (indicated by the square in panel C) with the Prx II residues labeled corresponding to the Prx I residues (which have residue numbers one greater than those of Prx II) that were mutated in this study.

which perhaps helps in orienting bound hSrx. The putative binding site includes the largest hydrophobic patch on the Prx surface (Figure 5B of the Supporting Information), implying an important role for hydrophobic hSrx−Prx interactions.

While the functional stoichiometry of hSrx bound to Prx in the cell has not yet been determined, hSrx is shown in panels A and B of Figure 6 bound to all 10 potential sites on the Prx decamer to illustrate the lack of contact between the individual bound hSrx proteins. This lack of contact suggests hSrx binding might be noncooperative, though the model cannot rule out allosteric effects. Nevertheless, perhaps just one hSrx protein is sufficient to reduce a sulfinic form Prx in the decamer.

Judging from the Cys−Cys and Cys−ATP distances, Cys51 of Prx would seem to be too distant for a reaction involving direct transfer of the γ-phosphate from ATP or from an hSrx Cys99 intermediate (Figure 7). Even with interactive manipulation of the docked structures, these distances could not be significantly reduced. Perhaps for proper function, hSrx must pry apart and insert into the Prx dimer−dimer interface. To test this possibility, docking to the Prx dimer subunit of the sulfinic form Prx decamer was also examined. The minimum Cys−Cys distance was reduced slightly to 11.9 Å, while the Cys51−γ-phosphate distance increased to 14.6 Å. Yet another possibility is that

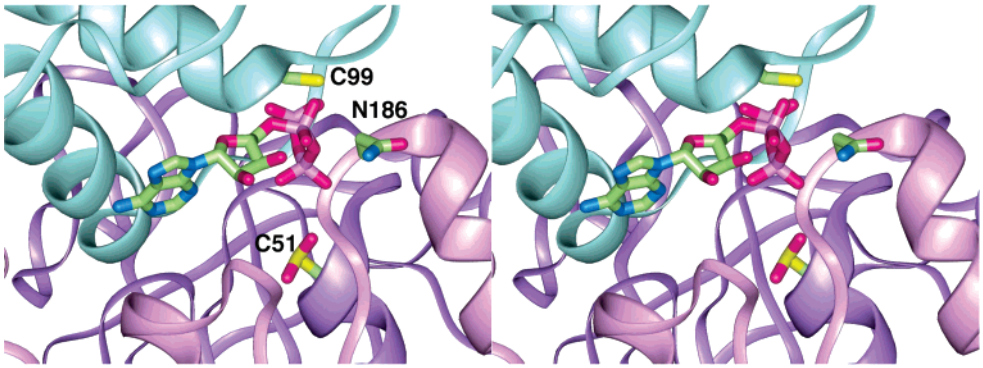

FIGURE 7: Stereo close-up view of the putative hSrx−Prx interface. The hSrx backbone is colored light blue, and two monomers of the Prx II decamer are colored pink and purple. The ATP bound to hSrx is shown. Its γ-phosphate lies less than 4 Å from the side chains of hSrx Cys99 and Prx II Asn186. The doubly oxidized Prx II Cys51 is also shown. While Cys51 appears close to the ATP phosphates and to hSrx Cys99 in this view, it is actually separated by more than 12 Å from both.

refolding occurs around Prx Cys51 during the reduction by hSrx, and since the oxidized form of Prx is folded differently to form the disulfide linkage, docking was also performed on the oxidized dimer Prx structure (*24*). In this case, EMAP failed to produce a docked structure similar to the sulfinic form Prx complexes, with a Cys−Cys distance no shorter than 14.2 Å and a Cys−ATP distance no shorter than 14.6 Å. Even when the structure of hSrx docked to the sulfinic form Prx dimer was superimposed onto the disulfide form Prx dimer, these distances were not significantly reduced, the Cys−Cys distance being 11.8 Å and the Cys−ATP distance 12.2 Å. Thus, in all three cases, docking to the sulfinic acid form Prx decamer, the dimer, and the disulfide form dimer, the model structures yielded large (~12 Å) Cys−Cys and Cys−ATP distances.

As a consistency check, docking was also performed with ClusPro. ClusPro evaluates billions of putative complexes with favorable surface complementarities and clusters and filters the output, selecting those with the best electrostatic and desolvation free energies (*25*, *33*). Because of size limits, only docking to the Prx dimer was performed, and the sulfinic form was used. Also, ClusPro is currently implemented only for standard amino acids, so ATP was not included. The ClusPro and EMAP docked structures were quite similar, with a backbone rms deviation of 5.5 Å.

Mutant Prx Binding and Activity. To test the validity of the docked structures yielding the shortest Cys−Cys and Cys−ATP distances, Prx I mutants were made by changing residues at or near the hypothetical hSrx−Prx interface, and binding to hSrx was assessed. The Prx mutations include E123A, R128A, and D146L mutations at the putative hSrx interface and the H169N mutation adjacent to the interface (Figure 6D). Residues R128, D146, and H169 are conserved for Prx I−IV but not Prx V and VI, and E123 is found just in Prx I and II. The E123A, R128A, and D146L mutations all interfered with hSrx binding, while the H169N mutation did not (Figure 8A).

As we described previously, hSrx has no catalytic residue such as aspartic acid near the β- or γ-phosphate groups of the bound ATP. By examining the model complex, we identified a suitable candidate residue, Prx II Asn186. Figure 7 shows a close-up of the model structure with Asn186 of Prx II, corresponding to Asp187 of Prx I, adjacent to the phosphates of the hSrx-bound ATP. This situation is reminiscent of Rap1, a Ras-like guanine nucleotide binding protein, which does not possess the catalytic glutamine essential for GTP hydrolysis. However, Rap1GAP (GTPase-activating protein), a Rap1-specific regulating protein, provides a catalytic asparagine for stimulating the hydrolysis of GTP utilizing a nucleophilic water molecule (*34*, *35*). Thus, we hypothesized that this Prx residue might act as the catalytic residue for hydrolysis of hSrx-bound ATP. Figure 9 shows the sequence alignment of the C-terminal region of the two-Cys class of Prx. As the figure shows, Prx I and Prx IV have a conserved aspartic acid. However, Prx II and Prx III have aspargine and serine, respectively.

To investigate whether this residue acts as the catalytic residue, we mutated Asp187 of Prx I to Ala, Asn, and Ser. We then measured the Prx-catalyzed hydrolysis of [γ-^{32}P]-ATP bound to hSrx and the reduction of the hyperoxidized form of wild-type Prx I and its mutants. The D187S mutant precipitated as an inclusion body; thus, we proceeded with the wild type and the D187A and D187N mutants of Prx I. As Figure 8 shows, although Prx I D187A binds hSrx with the same affinity as the wild type (Figure 8A), reduction of hyperoxidized Prx I (Figure 8B) and hydrolysis of [γ-^{32}P]-ATP were lost (Figure 8C,D). However, for Prx I D187N, these activities were almost the same as that for the wild type. These results suggest that these mutations do not affect the structure of the binding surface of Prx I with hSrx and that Asp187 acts as the catalytic residue for hydrolysis of ATP. Also, since the hydrolysis and reduction activities of the D187N mutant were comparable to those of the wild type, this suggests Asn186 is the catalytic residue of Prx II.

DISCUSSION

hSrx Structural Comparisons. Free and ADP-bound hSrx structures have been determined by X-ray crystallography (*36*). The X-ray and NMR structures are quite similar, with an average backbone rmsd of 0.9 Å between NMR ATP-bound hSrx and both X-ray structures and 1.0 Å between NMR free hSrx and both X-ray structures. The bound ATP base and ribose ring in the NMR structure are in the same location as the ADP base and ribose ring in the X-ray structure. The β-phosphate of the bound ADP is situated at the head of helix 2 and makes hydrogen bonds similar to those of the γ-phosphate in the NMR structures (Figure 5), though the ADP β-phosphate is necessarily nearer the ribose, so the exact positions of the ADP β-phosphate and ATP γ-phosphate differ by 2.6 Å. The largest difference between

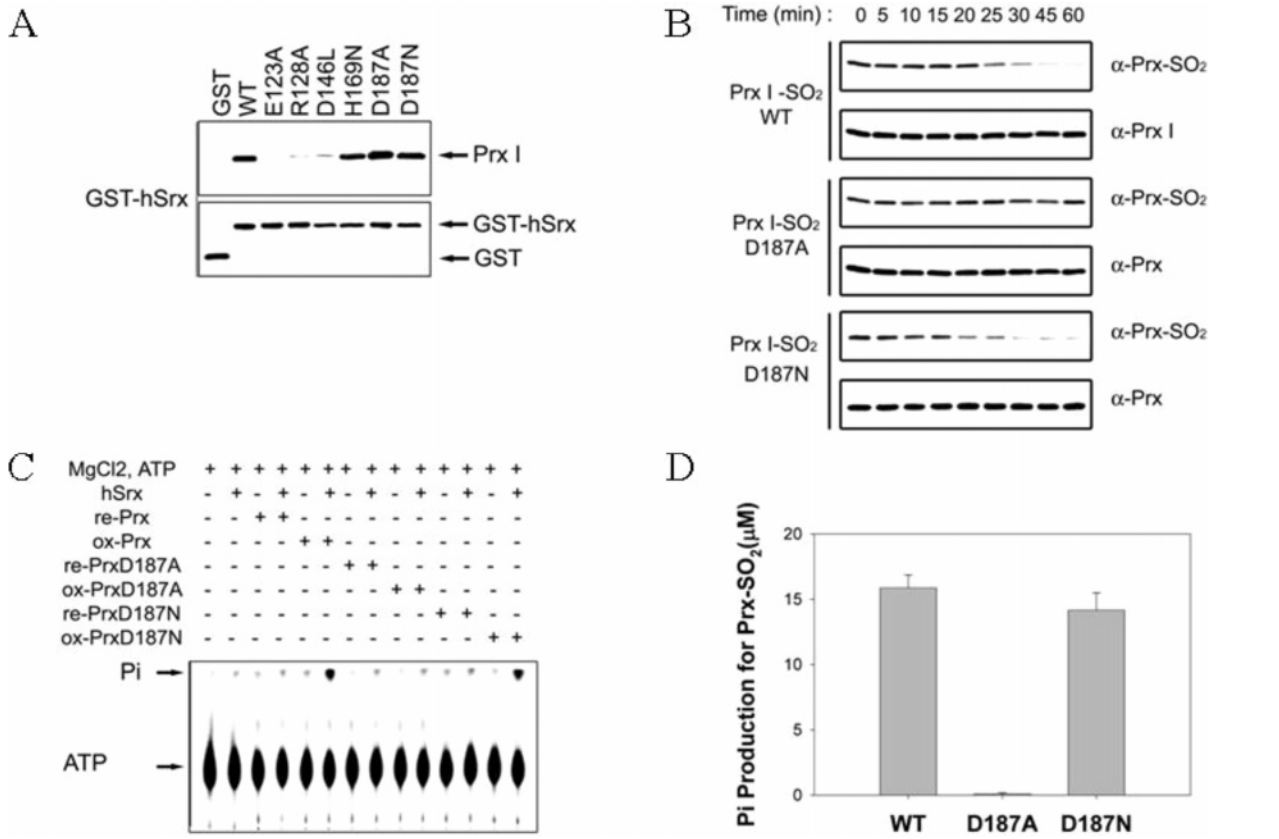

FIGURE 8: Activity of hSrx depending on the wild-type or mutant Prx protein. (A) Change in affinity of wild-type and mutant Prx I for hSrx. Wild-type and mutant Prx I proteins (1 μg) were each incubated for 2 h at 4 °C with either GST or the GST−hSrx fusion protein (5 μg) in 1 mL of binding buffer [50 mM HEPES buffer (pH 7.0), 150 mM NaCl, 1% Triton X-100, 1 mM EDTA, and 1 mM DTT]. Samples precipitated with GSH−Sepharose resins were subjected to immunoblot analysis with antibodies to Prx I or GST. (B) Reduction of sulfinic acid determined by immunoblot analysis with antibodies to cysteine and cysteinesulfinic acid. (C) Dephosphorylation due to interaction of Prx I with hSrx after 60 min shown by retention time difference on the TLC using polyethyleneimine (PEI). (D) Amount of γ-$^{32}P_i$ formed on the TLC plate, measured with a liquid scintillation counter. The reaction mixture containing 100 mM Tris-HCl (pH 7.5), 1 mM $MgCl_2$, 250 mM ATP [or added [γ-^{32}P]ATP (0.4 μCi/μL)], 10 mM GSH, 20 μM sulfinic Prx I, and 2 μM hSrx was incubated for the indicated time at 30 °C.

FIGURE 9: Alignment of the C-terminal sequences of human Prx I−IV. Conserved residues are shaded. The corresponding secondary structure is shown. Prx I Asp187 is denoted with a black star, and the resolving cysteine, which forms the disulfide linkage with the peroxidatic cysteine, is denoted with a white star.

the NMR and X-ray protein structures is seen in the vicinity of Val56, differing by 2.5 Å. Comparison of the NMR NOE spectra signals with the corresponding distances in the X-ray structures, between Val56 and Cys99 and His100, for instance, confirms that the solution structure must differ significantly from the crystal structure in this region. The reason for this difference is unclear, though it is interesting that it occurs at the predicted hSrx−Prx interface and next to residue Ser55, which has a large amide chemical shift change upon binding ATP and ADP.

The ability of hSrx to bind all di- and triphosphate nucleotides with only moderate base specificity (*6*) might be due to hSrx being tailored specifically to bind the terminal phosphate of the di- or triphosphate nucleotide. The flexible side chains of Lys61 and Arg101 can accommodate di- and triphosphate binding by adjusting their interactions with the phosphate groups, while the interactions of the terminal phosphate with the head of helix 2 and the His100 side chain remain similar.

A Dali structural similarity search revealed that hSrx has the parB domain fold, as already predicted on the basis of sequence analysis (*37*); in particular, hSrx is similar to a protein of unknown function from *Pyrococcus furiosus* (PDB entry 1VK1; backbone rmsd of 2.9 Å; *z* score of 6.6) and to the chromosomal segregation protein Spo0J of *Thermus thermophilus* (PDB entry 1VZ0; backbone rmsd of 2.9 Å; *z* score of 4.6). Whether these proteins bind ATP is not known. Both these proteins have an additional C-terminal domain. Superposing these two proteins on hSrx in the hSrx−Prx model shows considerable overlap in the position of the *P. furiosus* protein C-terminal domain and Prx, though Prx has more extensive contacts in the ATP phosphate binding region of hSrx than those seen in the corresponding interface region of the *P. furiosus* protein. Overlap between the C-terminal domain of Spo0J and Prx in the hSrx−Prx complex was less substantial. No structural similarity is seen between either C-terminal domain and Prx.

Reduction Mechanism and Structural Rearrangement. While the modeling and mutagenesis present compelling evidence for Prx I Asp187 being the catalytic residue in ATP hydrolysis, just how this hydrolysis is linked to the reduction

of the cysteinesulfinic acid is not clear. Cysteine 99 of hSrx in the active site likely plays a central role in the reduction mechanism (*32*). This cysteine lies in a region of strong positive electrostatic potential, lying adjacent to Arg51 and His100, as well as lying at the N-terminal end of helix II, lowering its pK_a (~7.3) and rendering it particularly reactive (*6*). A proposed intermediate in the reduction mechanism is cysteinyl phosphate, known from phosphatases (*38*), with hydrolysis transferring the γ-phosphate to Cys99 (*32*). In the ATP-bound hSrx structure, Cys99 lies just past the end of the triphosphate group, 4 Å from the γ-phosphate; thus, transfer of the phosphate to Cys99 appears plausible. Lying within the Prx−hSrx interface, the cysteinyl phosphate should be shielded from hydrolysis by solvent, giving it sufficient time to participate in the next step of the reduction mechanism.

In the model complex structures, hSrx Cys99 lies no less than 12 Å from the cysteinesulfinic acid residue of Prx; even after addition of the phosphoryl group to Cys99, the distance is still greater than 9 Å. If the cysteinyl phosphate is truly an intermediate in the reduction mechanism, then perhaps some structural rearrangment brings the cysteine residues closer together. Such rearrangement might not be needed for ATP hydrolysis since the catalytic Prx I Asp187 seems already well placed adjacent to the ATP β- and γ-phosphates. However, hydrolysis occurs only when Prx is in its sulfinic form, suggesting something more than simply placing Prx I Asp187 adjacent to the ATP phosphates is needed for hydrolysis to occur. The ATP- and ADP-bound structures of hSrx are quite similar, so hydrolysis alone does not seem to have a large effect on hSrx structure, at least for unbound hSrx. On the other hand, the differences between the NMR and X-ray structures for hSrx seen for Val56 on the loop that lies directly between hSrx Cys99 and the Prx cysteinesulfinic acid suggest this loop region could be structurally labile.

As for the Prx structure, for the disulfide bond to form after the initial oxidation, the helix containing the peroxidatic cysteine must partially unwind and the C-terminal region containing the resolving cysteine must unfold (*1*, *29*). Even though the structure of the cysteinesulfinic acid form of Prx more closely resembles the reduced form, the structural change needed to form the disulfide indicates a propensity for structural rearrangement in this region of Prx. A hint that such structural rearrangement occurs is the fact that mutation of hSrx Asp80 to Asn interferes with Prx binding. In the model complexes, Asp80 is roughly 6 Å from the hSrx−Prx interface. Intriguingly, Asp80 lies closest to the C-terminal helix of Prx, the part of Prx that must structurally rearrange to form the disulfide. Thus, while structural change might not be necessary for an initial hydrolysis step with Prx I Asp187 as the catalytic residue, it is plausible that at some point the reduction of the Prx cysteinesulfinic acid involves a major structural rearrangement at the complex interface, bringing the hSrx and Prx cysteines closer together.

SUPPORTING INFORMATION AVAILABLE

Additional figures and the statistics table mentioned in the text. This material is available free of charge via the Internet at http://pubs.acs.org.

REFERENCES

1. Wood, Z. A., Schroder, E., Harris, R. J., and Poole, L. B. (2003) Structure, mechanism and regulation of peroxiredoxins, *Trends Biochem. Sci. 28*, 32−40.
2. Rhee, S. G., Kang, S. W., Jeong, W., Chang, T. S., Yang, K. S., and Woo, H. A. (2005) Intracellular messenger function of hydrogen peroxide and its regulation by peroxiredoxins, *Curr. Opin. Cell Biol. 17*, 183−189.
3. Chae, H. Z., Chung, S. J., and Rhee, S. G. (1994) Thiodoxin-dependent Peroxide Reductase from Yeast, *J. Biol. Chem. 269*, 27670−27678.
4. Biteau, B., Labarre, J., and Toledano, M. B. (2003) ATP-dependent reduction of cysteine-sulphinic acid by *S. cerevisiae* sulphiredoxin, *Nature 42*, 980−984.
5. Rhee, S. G., Yang, K. S., Kang, S. W., Woo, H. A., and Chang, T. S. (2005) Controlled elimination of intracellular H_2O_2: Regulation of peroxiredoxin, catalase, and glutathione peroxidase via post-translational modification, *Antioxid. Redox Signaling 7*, 619−626.
6. Chang, T. S., Jeong, W., Woo, H. A., Lee, S. M., Park, S., and Rhee, S. G. (2004) Characterization of mammalian sulfiredoxin and its reactivation of hyperoxidized peroxiredoxin through reduction of cysteine sulfinic acid in the active site to cysteine, *J. Biol. Chem. 279*, 50994−51001.
7. Wu, X. W., Milne, J. L., Borgnia, M. J., Rostapshov, A. V., Subramaniam, S., and Brooks, B. R. (2003) A core-weighted fitting method for docking atomic structures into low-resolution maps: Application to cryo-electron microscopy, *J. Struct. Biol. 141*, 63−76.
8. Milne, J. L., Wu, X. W., Borgnia, M. J., Lengyel, J. S., Brooks, B. R., Shi, E., Perham, R. N., and Subramaniam, S. (2002) Molecular architecture and mechanism of an icosahedral pyruvate dehydrogenase complex: A multifunctional catalytic machine, *EMBO J. 21*, 5587−5598.
9. Lee, D. Y., Rhee, S. G., Ferretti, J. A., and Gruschus, J. M. (2005) ^{1}H, ^{15}N, and ^{13}C chemical shift assignments of the human Sulfiredoxin (hSrx), *J. Biomol. NMR 32*, 339.
10. Gruschus, J. M., and Ferretti, J. A. (1999) Signal enhancement using 45 degrees water flipback for 3D ^{15}N-edited ROESY and NOESY HMQC and HSQC, *J. Magn. Reson. 140*, 451−459.
11. Vuister, G. W., and Bax, A. (1992) Measurement of two-bond JCOH α coupling constants in proteins uniformly enriched with ^{13}C, *J. Biomol. NMR 2*, 401−405.
12. Muhandiram, D. R., and Kay, L. E. (1994) Gradient-enhanced triple-resonance three-dimensional NMR experiments with improved sensitivity, *J. Magn. Reson., Ser. B 103*, 203−216.
13. Ikura, M., Kay, L. E., and Bax, A. (1990) A novel approach for sequential assignment of ^{1}H, ^{13}C, and ^{15}N spectra of proteins: Heteronuclear triple-resonance three-dimensional NMR spectroscopy. Application to calmodulin, *Biochemistry 29*, 4659−4667.
14. Grzesiek, S., and Bax, A. (1993) Measurement of amide proton exchange rates and NOEs with water in ^{13}C/^{15}N-enriched calcineurin B, *J. Biomol. NMR 3*, 627−638.
15. Piotto, M., Saudek, V., and Sklenar, V. (1992) Gradient-tailored excitation for single-quantum NMR spectroscopy of aqueous solutions, *J. Biomol. NMR 2*, 661−665.
16. Garrett, D. S., Seok, Y. J., Peterkofsky, A., Clore, G. M., and Gronenborn, A. M. (1997) Identification by NMR of the binding surface for the histidine-containing phosphocarrier protein HPr on the N-terminal domain of enzyme I of the *Escherichia coli* phosphotransferase system, *Biochemistry 36*, 4393−4398.
17. Delaglio, F., Grzesiek, S., Vuister, G. W., Zhu, G., Pfeifer, J., and Bax, A. (1995) NMRPipe: A multidimensional spectral processing system based on UNIX pipes, *J. Biomol. NMR 6*, 277−293.
18. Wishart, D. S., and Sykes, B. D. (1994) The ^{13}C chemical-shift index: A simple method for the identification of protein secondary structure using ^{13}C chemical-shift data, *J. Biomol. NMR 4*, 171−180.
19. Gruschus, J. M., Han, C. J., Greener, T., Ferretti, J. A., Greene, L. E., and Eisenberg, E. (2004) Structure of the functional fragment of auxilin required for catalytic uncoating of clathrin-coated vesicles, *Biochemistry 43*, 3111−3119.
20. Cornilescu, G., Delaglio, F., and Bax, A. (1999) Protein backbone angle restraints from searching a database for chemical shift and sequence homology, *J. Biomol. NMR 13*, 289−302.

21. Schwieters, C. D., Kuszewski, J. J., Tjandra, N., and Clore, G. M. (2003) The XPLOR-NIH NMR molecular structure determination package, *J. Magn. Reson. 160*, 65−73.
22. Folmer, R. H., Hilbers, C. W., Konings, R. N., and Nilges, M. (1997) Floating stereospecific assignment revisited: Application to an 18 kDa protein and comparison with J-coupling data, *J. Biomol. NMR 9*, 245−258.
23. Schroder, E., Littlechild, J. A., Lebedev, A. A., Errington, N., Vagin, A. A., and Isupov, M. N. (2000) Crystal structure of decameric 2-Cys peroxiredoxin from human erythrocytes at 1.7 Å resolution, *Struct. Folding Des. 8*, 605−615.
24. Hirotsu, S., Abe, Y., Okada, K., Nagahara, H., Hori, H., Nishino, T., and Hakoshima, T. (1999) Crystal structure of a multifunctional 2-Cys peroxiredoxin heme-binding protein 23 kDa/proliferation-associated gene product, *Proc. Natl. Acad. Sci. U.S.A. 96*, 12333−12338.
25. Comeau, S. R., Gatchell, D. W., Vadja, S., and Camacho, C. J. (2004) ClusPro: An automated docking and discrimination method for the prediction of protein complexes, *Bioinformatics 20*, 45−50.
26. Cerdan, R., Payet, D., Yang, J. C., Travers, A. A., and Neuhaus, D. (2001) HMG-D complexed to a bulge DNA: An NMR model, *Protein Sci. 10*, 504−518.
27. Adams, P. D., Loh, A. P., and Oswald, R. E. (2004) Backbone dynamics of an oncogenic mutant of Cdc42Hs shows increased flexibility at the nucleotide-binding site, *Biochemistry 43*, 9968−9977.
28. Guvench, O., Shenkin, P., Kolossvary, I., and Still, W. C. (2002) Application of the frozen atom approximation to the GB/SA continuum model for solvation free energy, *J. Comput. Chem. 23*, 214−221.
29. Wood, Z. A., Poole, L. B., Hantgan, R. R., and Karplus, P. A. (2002) Dimers to doughnuts: Redox-sensitive oligomerization of 2-cysteine peroxiredoxins, *Biochemistry 41*, 5493−5504.
30. Wood, Z. A., Poole, L. B., and Karplus, P. A. (2003) Peroxiredoxin evolution and the regulation of hydrogen peroxide signaling, *Science 300*, 650−653.
31. MacKerell, A. D., Jr., Brooks, B., Brooks, C. L., III, Nilsson, L., Roux, B., Won, Y., and Karplus, M. (1998) CHARMM: The energy function and its parametrization with an overview of the program, in *The Encyclopedia of Computational Chemistry* (Schleyer, P. v. R., Ed.) pp 271−277, John Wiley & Sons, Chichester, U.K.
32. Jeong, W., Park, S. J., Chang, T. S., Lee, D. Y., and Rhee, S. G. (2006) Molecular mechanism of the reduction of cysteine sulfinic acid of peroxiredoxin to cysteine by mammalian sulfiredoxin, *J. Biol. Chem. 281*, 14400−14407.
33. Comeau, S. R., Gatchell, D. W., Vadja, S., and Camacho, C. J. (2004) ClusPro: A fully automated algorithm for protein-protein docking, *Nucleic Acids Res. 32*, W96−W99.
34. Nassar, N., Hoffman, G. R., Manor, D., Clardy, J. C., and Cerione, R. A. (1998) Structures of Cdc42 bound to the active and catalytically compromised forms of Cdc42GAP, *Nat. Struct. Biol. 5*, 1047−1052.
35. Daumke, O., Weyand, M., Chakrabarti, P. P., Vetter, I. R., and Wittinghofer, A. (2004) The GTPase-activating protein Rap1GAP uses a catalytic asparagines, *Nature 429*, 197−201.
36. Jonsson, T. J., Murray, M. S., Johnson, L. C., Poole, L. B., and Lowther, W. T. (2005) Structural basis for the retroreduction of inactivated peroxiredoxins by human sulfiredoxin, *Biochemistry 44*, 8634−8642.
37. Basu, M. K., and Koonin, E. V. (2005) Evolution of eukaryotic cysteine sulfinic acid reductase, sulfiredoxin (Srx), from bacterial chromosome partitioning protein ParB, *Cell Cycle 4*, 947−952.
38. Wo, Y. Y. P., Zhou, M. M., Stevis, P., Davis, J. P., Zhang, Z. Y., and Vanettern, R. L. (1992) Cloning, expression, and catalytic mechanism of the low-molecular-weight phosphotyrosyl protein phosphatase from bovine heart, *Biochemistry 31*, 1712−1721.

BI061824H